

The Narrow Gate: Localized Image-Text Communication in Vision-Language Models

Alessandro Pietro Serra^{1,2*} Francesco Ortu^{1,3*} Emanuele Panizon^{1*} Lucrezia Valeriani^{1,3}

Lorenzo Basile^{1,3} Alessio Ansuini¹ Diego Doimo^{1†} Alberto Cazzaniga^{1†}

¹ AREA Science Park, Trieste, Italy

² SISSA, Trieste, Italy

³ University of Trieste, Trieste, Italy

{diego.doimo, alberto.cazzaniga}@areasciencepark.it

Abstract

*Recent advances in multimodal training have significantly improved the integration of image understanding and generation within a unified model. This study investigates how vision-language models (VLMs) handle image-understanding tasks, specifically focusing on how visual information is processed and transferred to the textual domain. We compare VLMs that generate both images and text with those that output only text, highlighting key differences in information flow. We find that in models with multimodal outputs, image and text embeddings are more separated within the residual stream. Additionally, models vary in how information is exchanged from visual to textual tokens. VLMs that only output text exhibit a distributed communication pattern, where information is exchanged through multiple image tokens. In contrast, models trained for image and text generation tend to rely on a single token that acts as a narrow gate for visual information. We demonstrate that ablating this single token significantly deteriorates performance on image understanding tasks. Furthermore, modifying this token enables effective steering of the image semantics, showing that targeted, local interventions can reliably control the model's global behavior.*¹

1. Introduction

The rise of foundation models [1] trained on vast amounts of text has transformed natural language processing (NLP),

showing that a single large language model (LLM) [2] can handle many different linguistic tasks [3–5]. The rich set of features encoded in LLM embeddings has been then used as an effective prior knowledge both for text-conditional image generation [6–8] and image understanding [9–13]. Recently, the availability of large open datasets [14, 15] and improved techniques to align text and image embeddings [16] have also enabled the creation of multimodal models that can both understand and generate visual content within a single architecture [17–20]. This unification allows a richer understanding of the visual world, as generative tasks often require insight into the fundamental concepts and relationships within the data [21]. For example, a model that generates images from text descriptions must grasp the semantic content of those images to ensure they faithfully reflect the details and intent of the text [22, 23]. As a result, research has rapidly progressed to integrate multiple modalities into a unified framework with increasingly deeper multimodal fusion.

Early approaches used cross-attention modules between modality-specific encoders [17]. Further advancements highlighted the importance of using a pre-trained LLM backbone combined with lightweight projection layers, often fine-tuning the LLM to refine the multimodal representations [19, 24, 25]. More recently, research has shown success in training multimodal-output vision-language models (VLMs) from scratch [20, 26], achieving performance close to VLMs that only output text on visual understanding tasks.

While recent studies have examined the internal mechanisms of unimodal-output VLMs [27–30], little to none is known about how different modalities interact in the hidden representations of multimodal-output models or whether

*Equal contribution

†Equal supervision

¹Code and data: <https://ritareasciencepark.github.io/Narrow-gate>

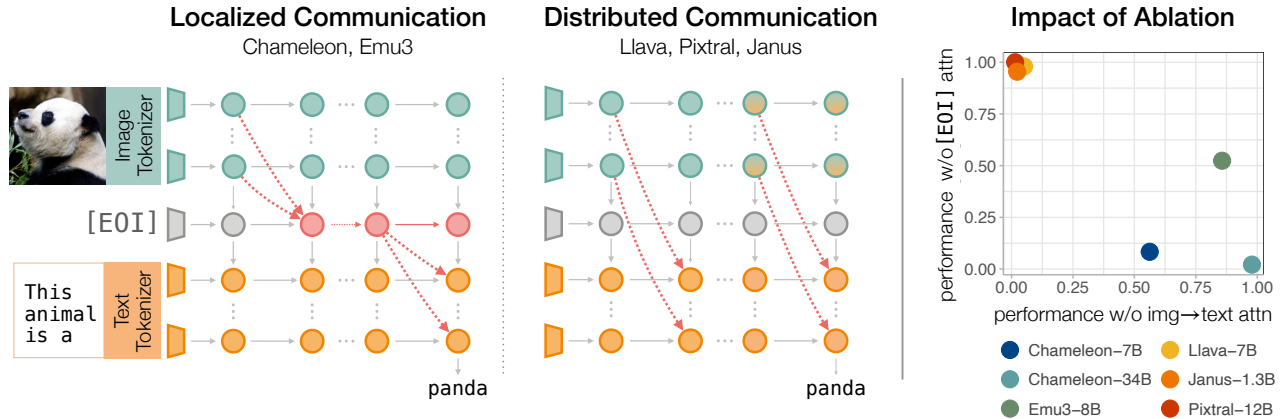


Figure 1. **Image-Text Communication in VLMs.** Different VLM designs handle information flow between modalities in radically different ways. Chameleon and Emu3 (left-panel), early-fusion and multimodal-output models, encode visual and textual tokens in separated regions, and knowledge transfer from image to text happens through a *narrow gate*, the end-of-image token [EOI]. On the contrary, in models like Llava (center-panel) designed for text generation, the image-text communication is distributed across many internal image tokens that directly communicate with the textual ones, and late-layer visual tokens tend to align more text tokens in the embedding space. The right panel shows that when a narrow gate is present, ablating the attention given by textual tokens to [EOI] has a stronger impact on performance than ablating the whole image-text attention. Results refer to image captioning on MS-COCO and are expressed as a fraction of performance without any ablation (Sec. 4.3 and Tab. 1).

their information processing resembles that of text-only VLMs. In this work, we focus on some of the latest early-fusion multimodal-output VLMs, Chameleon [20] and Emu3 [26], and compare them with a range of unimodal-output VLMs, such as Llava [11], on how they transfer information from the visual domain to the textual domain in various image understanding tasks.

In Chameleon and Emu3, we observe that image and text representations remain well separated in different clusters from input to output, while in models like Llava they tend to mix in late layers (Sec. 4.1). Additionally, in Llava the information flow from image to text is distributed across multiple tokens. In contrast, multimodal-output VLMs channel the global image information into a single token placed immediately after the image, which we refer to as the *end-of-image token*, denoted by [EOI] (Sec. 4.2). The [EOI] token behaves like a memory token [31] or “narrow gate” through which the image information must pass to guide text generation.

We experimentally demonstrate the crucial role of [EOI], by showing that (1) if we block information flow from [EOI] to textual tokens, model performance dramatically drops across a variety of tasks, including image classification, visual question answering (VQA), and image captioning (see Sec. 4.3); (2) if we edit the information stored in [EOI], we can change the image semantics and its textual description (see Sec. 4.4).

None of these properties hold for Llava and other

unimodal-output VLMs, where the information between modalities flows through many distributed image tokens specialized for cross-modal communication.

2. Related Works

Multimodal Vision Language Models. Many approaches have been proposed to adapt decoder-only LLMs trained with autoregressive loss for image understanding [10–13, 32, 33] and multimodal generation tasks [16, 19–21, 24–26, 34–37]. These models consist of an LLM, an image encoder, an image decoder (for multimodal-output VLMs), and adapters between the LLM and visual components. The success of diffusion-based image generation has led to the widespread use of stable diffusion as the decoding architecture in multimodal-output models [16, 19, 21, 24, 25, 35]. For the image encoding part, most architectures use a vision transformer (ViT), often that of CLIP [16, 19, 21, 24, 25, 34–36], due to the effectiveness of ViT embeddings in encoding image semantics [38]. The outputs from the visual encoder are either directly projected into the LLM embedding space [21, 24, 25, 38] or, in the case of multimodal generation, often mapped to a discrete set of tokens [16, 19, 34]. A drawback of these methods is the complexity of encoding architecture. Moreover, the image-text contrastive loss can make the image representations resemble textual ones excessively [33], with text often favored as the preferred modality [17, 19, 25]. Alternative approaches use VQ-VAEs [39, 40] to encode and decode the images and train the LLMs from

scratch on multimodal datasets [20, 26]. This strategy fuses the visual and textual representations early in training instead of using complex pipelines to bridge the modality gap [32, 38, 41, 42] and eliminates the need for adapters, greatly simplifying the architecture design.

Special Tokens, Memory Tokens, Registers. The importance of special tokens to store and redistribute global information was emphasized by Burtsev et al. [31]. In their work, they add these special tokens at the beginning of the sequence to serve as memory units accessible through the self-attention mechanism, improving performance on various language processing tasks. In vision transformers, Darcey et al. [43] found that high-norm tokens in low-informative areas of the images are used to store global information while discarding the local one. Adding learnable “register tokens” dedicated to global information processing helped eliminate the high-norm artifacts, improving performance. Similarly, Wen et al. [29] used learnable registers to summarize salient visual information and remove the image tokens altogether, improving the efficiency of vision-language models.

Information Flow in Text-Only VLMs. In text-only VLMs, this summarization is particularly useful since much of the attention to image tokens is concentrated in the initial layers, likely on a few “anchor tokens” [28, 44]. Basu et al. [28] demonstrated with multimodal causal tracing that, in VQA tasks, a subset of strongly attended *late image tokens* in early layers transfer information to the text. However, a later ablation study by Neo et al. [27] showed that important information about objects is often localized in tokens corresponding to the object’s position in the image. Interestingly, they also observed that image tokens — which may have different statistical properties compared to textual tokens [45] — in the deeper layers encode vocabulary words that describe the objects they belong to.

3. Background and Methods

3.1. Model Architectures

This study explores how multimodal-output and text-only output VLMs exchange information between visual and textual tokens. We focus on models that fuse image and text tokens from the start of training and can generate images and text within the same architecture. Chameleon [20] and Emu3 [26] serve as representatives of this class. Since Wang et al. [26] released two fine-tuned versions of Emu3 – Emu3-Gen for image generation and Emu3-chat for image understanding – we fine-tune Emu3-Gen on a mixture of image-text datasets to perform well on both tasks. This enables a direct comparison with Chameleon, which natively supports the joint generation of images and text. Fine-tuning details for Emu3 are provided in the Supplementary Material

(SM) in Sec. 7.1. For text-only output VLMs, we analyze Llava-onevision-7B [46] and Pixtral-12B [13], fine-tuned on Qwen2-7B and Mistral Nemo 12B, respectively. Additionally, we also analyze Janus-1.3B [36], a multimodal-output model *fine-tuned* on a DeepSeek-LLM backbone. Janus uses a SigLIP image encoder and retains the pre-trained unembedding matrix for text generation. Unlike Chameleon and Emu3, which use a unified VQ-GAN encoder-decoder for multimodal tasks, Janus has an encoding-decoding structure specialized in image understanding tasks which is different from the one used for image generation. This makes its architecture closer to Llava and Pixtral.

All the models are decoder-only and trained with next-token prediction loss. In Chameleon, Emu3, and Janus, the loss is computed on both image and text tokens, while in Llava-onevision and Pixtral, it applies only to text tokens. In all the cases, a special end-of-image token ($[EOI]$) marks the transition from image to text. Additional details of the model architectures is provided in Table SM3 of the Supplementary Material.

3.2. Datasets and Representations

We analyze visual understanding tasks where the model generates answers for VQAv2 [47], image descriptions for Flickr30k [48] and MS-COCO [49], or completes simple prompts describing ImageNet [50] images. Detailed experimental settings, including dataset composition, evaluation metrics, prompt usage, and data selection criteria are described in the SM Sec. 7.

To study how VLMs process information, we examine attention maps and token representations at the output of each attention block. We denote x_i^l as the representation of a token at the i^{th} position of the sequence at layer l , before layer norm. Following [51], we refer to x_i^l as the *residual stream* of the token t_i at layer l . Most experiments use prompts in a consistent format: an image followed by a textual prompt. This motivates the definition of the following matrix blocks. Let $N_{[EOI]}$ be the index of the end-of-image token and $A_{i,j}$ the attention weight between token i and j . We define:

1. $A_{img} = A_{i,j}$ with $1 \leq i < N_{[EOI]}, 0 < j < N_{[EOI]}$: image self-attention;
2. $A_{text} = A_{i,j}$ with $N_{[EOI]} < i \leq N, N_{[EOI]} < j \leq N$: text self-attention;
3. $A_{img \rightarrow text} = A_{i,j}$ with $N_{[EOI]} < i \leq N, 0 < j < N_{[EOI]}$: communication between text and image;
4. $A_{target \rightarrow text} = A_{i,j}$ with $N_{[EOI]} < i \leq N, j = N_{target}$: column of A associated with a specific *target token*.

3.3. Analytical Tools

Quantification of Cross-Modal Attention. We construct a metric that quantifies the average attention that all the text tokens give to a token at position j within the image part of

the prompt, which we assume to span the first $N_{[\text{EOI}]}$ tokens. Formally, we define the (relative) *cross-modal attention* f_j^l as

$$f_j^l = \frac{1}{C} \frac{1}{|\mathcal{H}|} \sum_{h \in \mathcal{H}} \sum_{i > N_{[\text{EOI}]}} A_{(i,j)}^{l,h} \quad (1)$$

Where $j = 0, 1, \dots, N_{[\text{EOI}]}$, l, h identify, respectively, the layer and head, and $A_{i,j}$ denotes the attention from the i^{th} to the j^{th} token. C is a normalization factor such that $\sum_{j \leq N_{[\text{EOI}]}} f_j^l = 1$.

Attention Knockout. We use the *attention knockout* technique introduced in [52], which selectively blocks attention between certain tokens at selected model layers. Given a set of source tokens \mathcal{S} and a set of target tokens \mathcal{T} , we prevent the target tokens from attending to the source tokens by zeroing out the corresponding entries, $\alpha_{(i,j)}$, in the attention matrix, where $i \in \mathcal{S}$ and $j \in \mathcal{T}$. This intervention is applied across all attention heads within the specified layers.

Neighborhood Overlap. Given a residual representation $\{x_i^l\}$ of n data points at layer l we denote by $\mathcal{N}^l(i)$ the set of k -nearest neighbors of the i -th vector x_i^l . Let us now consider an arbitrary labeling $\{y_i\}$ of the same data, referred to as its ground truth. We assess how well the geometric arrangement of the representations $\{x_i^l\}$ aligns with the labels $\{y_i\}$ by employing the neighborhood overlap (NO) quantity introduced by [53]. Intuitively, the NO, represented as $\chi^{l,gt}$, is the average fraction of k -nearest neighbors for each representation vector that share the same label, calculated across the entire dataset. More formally, defining a ground truth adjacency matrix as follows: $A_{ij}^{gt} = 1$ if $y_i = y_j$ and 0 otherwise, the NO of $\{x_i^l\}$ with the labeling $\{y_i\}$ can be written as:

$$\chi^{l,gt} = \frac{1}{n} \sum_i \frac{1}{k} \sum_{j \in \mathcal{N}^l(i)} A_{ij}^{gt} \quad (2)$$

In this work, we will use NO as a *semantic probe* to quantify the information content in the residual stream. For all of the following experiments we will be using $k = 30$.

Activation Patching. To evaluate the effect of specific model components on predictions, we adopt the *activation patching* technique, widely used in prior works [54, 55]. This approach involves two forward passes on two different inputs: first, we collect target activations \hat{x}_i^l ($\hat{x}_{i,\text{in}}^l$) at a given position i and layer l from the first input. Then, while processing a second input, we replace the base activation x_i^l ($x_{i,\text{in}}^l$) with the target activation \hat{x}_i^l ($\hat{x}_{i,\text{in}}^l$). By measuring the impact on the model’s final prediction, we quantify the influence of different model components on its generative process. We quantify the effect of these interventions by measuring the similarity between the output probability

distribution of the target (p_{target}) inputs and the probability distribution of the base inputs after patching ($q_{\text{base}}^{\text{patched}}$). The similarity measure is calculated using a variant of the Jaccard index [56], defined as:

$$\text{Similarity}(q_{\text{base}}^{\text{patched}}, p_{\text{target}}) = \sum_i \min(q_i, p_i) \quad (3)$$

This score quantitatively measures how closely the modified model output aligns with the target distribution after activation patching. The score is 1 if p and q are identical and 0 if their supports are fully disjoint.

Reproducibility. To perform our experiments we employed HuggingFace implementations of the 34B and 7B versions of Chameleon [57, 58], Emu3-Gen [59], Llava-7B [60], Pixtral-12B [61] and Janus-1.3B [62] models. All the experiments were executed on a single NVIDIA A100 GPU equipped with 40GB VRAM, except for the experiments on Chameleon-34B, which were performed using two A100 with 40GB VRAM each. We will release the code and data to reproduce the experiments upon acceptance of this work.

4. Results

4.1. Modality Gap in Multimodal-Output VLMs

Multimodal-output VLMs can generate image and text tokens within the same transformer backbone. Thus, they leverage shared parameters to perform the next token prediction task on all modalities in a unified representation space. In contrast, unimodal-output VLMs generate textual tokens using image tokens only as contextual information. Although both types of VLMs encode in the residual stream both image and text tokens, the role of each modality in the generation process differs significantly. This observation leads us to investigate whether models that generate both modalities favor the emergence of modality-specific regions of the residual stream space that separate image and text representations.

To address this question, we randomly select 10,000 image-caption pairs from the Flickr30k dataset. To consider the effect of conditional generation in both modalities, we construct 10,000 prompts with an image followed by text and 10,000 prompts with reverse ordering. We then perform a forward pass through the model, storing hidden representations in the residual stream for each modality across all layers. For any image-text pair, we extract the hidden representations at a randomly chosen *text token position*. When the order is reversed (text before image), we focus on the representations at a randomly chosen *image token position*. Details on prompt construction are provided in SM Sec. 7.

We compare the geometric organization of the different modalities by measuring the median cosine similarity

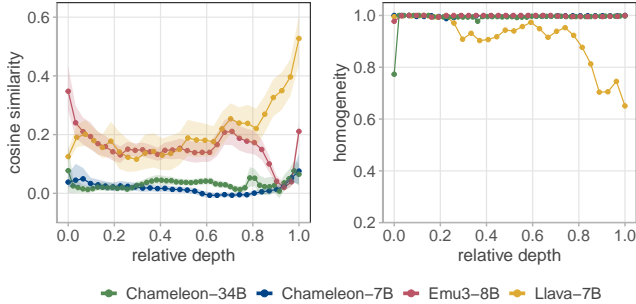


Figure 2. **Modality Gap in VLMs.** (left) Cosine similarity between text and image token embeddings as a function of model depth reflects their increasing alignment for the Llava model. In contrast, modalities do not align for the Emu3 model, and they are stably orthogonal for Chameleon. Points represent median cosine similarity, with shaded areas indicating the interquartile range. (right) Homogeneity score of token clusters generated via Advanced Density Peaks with respect to their original modality.

between representations of image and text tokens in hidden layers. Fig. 2 (left) shows the cosine similarity for Chameleon-7B (blue), Chameleon-34B (green), Emu3-8B (red) and Llava-7B (yellow). In Chameleon models, the representative vectors of image and text tokens remain nearly orthogonal across the hidden layers, with median cosine similarity values below 0.1. The cosine similarity in Llava and Emu3 is higher, starting at 0.2 in the initial layers of the network. While in Llava it then rises to 0.5 in the final layers, in Emu3 it falls towards 0 in the final region, with an upward tick in the last layer only. Llava’s upward trend suggests that the two modalities increasingly mix in later layers, while the opposite happens in Emu3, where the representations increasingly separate towards the end of the model.

To further investigate the degree of mixture of modalities in different models, we apply the Advanced Density Peaks clustering method [63] (see SM Sec. 7.5 for a brief introduction) and analyze the composition of each cluster. Fig. 2 (right) shows the homogeneity score [64] of the clusters, measuring how the clustering of tokens aligns with their modality. In Chameleon and Emu3 models (green, blue and red profiles), the homogeneity score is always 1, meaning that each cluster contains embeddings coming from a single modality. In contrast, Llava’s homogeneity score decreases from almost 1 to approximately 0.6 in the later layers of the network, indicating a tendency for the text and image embeddings to mix. In SM Sec. 6.1, Fig. SM1 shows the profiles of the cosine similarity and homogeneity for Janus and Pixral. These models behave similarly to Llava with a tendency to develop representations in which textual and image tokens are mixed toward the output of the LLMs.

We conclude that textual and visual representation spaces are largely separated in the Chameleon and Emu3 models, which are the only ones trained from scratch on multimodal

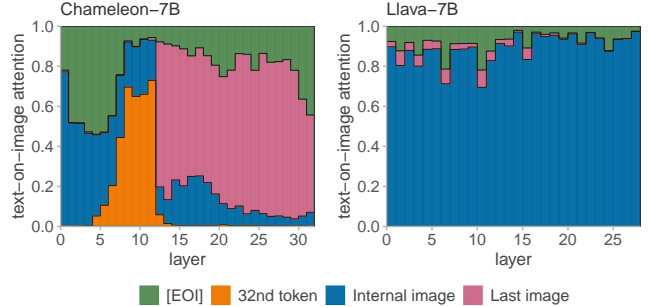


Figure 3. **Cross-Modal Attention Contributions of Image Tokens.** Contribution of different image token positions to the total text-on-image attention across layers in Chameleon-7B (left) and Llava-onevision-7B (right), computed on ImageNet data. Tokens with an average contribution larger than 1% are singled out. The remaining tokens are aggregated as “internal image”.

data and can effectively generate images and textual samples. This brings forth the problem of finding how and where communication between the two modalities is performed.

4.2. Analysis of Cross-Modal Attention

As shown in Sec. 4.1, hidden representations of visual and textual tokens are mixed in late layers of text-output models. At the same time, they pertain to well-separated regions of the residual stream in multimodal-output models. Despite this structural difference, both model types achieve good performance in image understanding tasks, suggesting that attention maps effectively transfer semantic information from the image to the text. To achieve this, the attention matrices play an important role: while sharing information among modalities, they need to bridge the modality gap, especially in Chameleon and Emu3 models. These observations lead us to define two fundamental features for tokens to efficiently handle cross-modal communication: *i*) having a large weight in the text-image attention and *ii*) having a rich semantic knowledge of the image. In the following, we investigate whether the Chameleon and Llava models - taken as examples for their respective classes of VLMs - have tokens that satisfy both requirements, thus being candidates for the role of communication *gate* between modalities. An identical analysis for all other models is shown in Fig. SM2

Cross-Modal Attention Patterns. To quantify the role of each token in image-to-text semantic communication, we use the ImageNet dataset and select 100 images per class for 100 animal classes [50]. We construct 10,000 prompts of images followed by text of the form “<image> This animal is a __”. The sentence was chosen to guide the model towards generating a class-relevant response. For the full list of classes, please refer to SM Sec. 7.

Fig. 3 illustrates the relative text-on-image attention, as defined in Sec. 3.3, at different token positions. We single

out tokens with an average value larger than 1%. The remaining tokens are aggregated as *internal image*. In the left panel, we show the distribution for Chameleon-7B. The special [EOI] token captures over 40% of the cross-modal attention in layers 2 to 6, with the remaining attention distributed among the other 1024 image tokens. In the middle layers, the [EOI] maintains a contribution between 8% and 12%, which increases again to over 37% in the final two layers. The last token of the image sequence also shows significant attention, contributing between 66% and 86% in the middle and final layers. Notably, the 32nd image token dominates attention between layers 7 and 11, peaking at over 60% between layers 8 and 11. The contribution from the remaining image tokens stays below 28% from layer 8 onward, progressively decreasing to less than 10% after layer 26. In the right panel, we present the distribution of average attention among tokens in Llava-onevision-7B. The [EOI] token account for approximately 10 – 20% of the attention between layers 0 and 13, and less than %10 for the remaining layers. All the remaining attention is distributed across the other image tokens.

In Fig. SM2 we report the attention distribution for Chameleon-34B, Emu3, Janus and Pixtral. In all the cases, the tokens with an average value larger than 1% include [EOI], the last image token, and special tokens indicating the end-of-lines [EOL] in Pixtral or storing the image sizes in Emu3.

Neighborhood Overlap of Embeddings. The analysis of total attention contributions reveals that a few localized tokens are strongly attended by text tokens, such as the [EOI], the 32nd and last image tokens in Chameleon-7B, and - less significantly - the [EOI] token in Llava-7B.

To investigate whether these tokens contain semantic visual information, we probe their hidden representations using the neighborhood overlap (see Sec. 3.3) with the ImageNet labels ($\chi^{l,gt}$), averaging across token positions when considering multiple tokens. Fig. 4 (left) shows that, in Chameleon-7B, the representation of the [EOI] token starts with a $\chi^{l,gt}$ near 0 in the first five layers and then rapidly increases, exceeding 0.4 from layer 9 to the end of the network. In contrast, the representations at the 32nd and last image tokens remain near 0 across all layers. This suggests that these positions do not encode meaningful visual information about the image. The representations of the image tokens inside the image increase from a $\chi^{l,gt}$ of 0 in the initial layers to approximately 0.2 at the 8th layer but gradually decrease, falling below 0.1 from layer 15 onward. These findings indicate that in Chameleon-7B, most image token positions contribute to encoding visual information in the early layers. Still, beyond the 8th layer, only the representation at the [EOI] token position retains meaningful information about the image. Similar results hold for Chameleon-34B

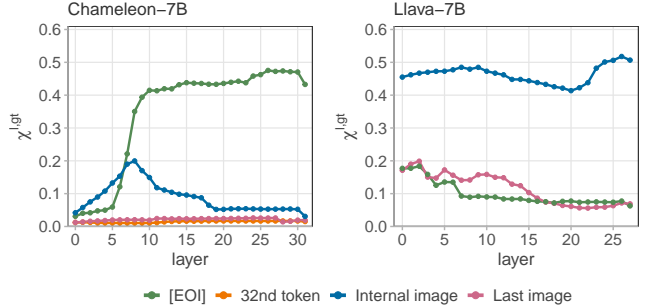


Figure 4. **Localization of Visual Semantic Information.** Neighborhood overlap between selected image tokens and ImageNet labels for Chameleon-7B (left) and Llava-7B (right). The blue curves are obtained by averaging over all internal image tokens excluding the 32nd token for the case of Chameleon.

and Emu3-8B, and are reported in Fig. SM2: the hidden representations of the [EOI] token achieve $\chi^{l,gt} > 0.4$ after layer 16 in Chameleon-34B and $\chi^{l,gt} > 0.3$ after layer 10 in Emu3-8B, while the other visual tokens have respectively overlap below 0.25 and 0.05 throughout the network.

In contrast, as shown in Fig. 4 (right), in Llava-7B, the representations of the token [EOI] start at a value of $\chi^{0,gt} \sim 0.20$ but drop below 0.10 at the later stage of the model, while the internal image tokens consistently stay at a higher $\chi^{l,gt} > 0.40$ across layers. The initial overlap of all tokens at layer 0 is consistent with the fact that the visual encoder of Llava-7B (SigLIP) already possesses meaningful visual features even at the earliest stages of the language model. This qualitative picture holds also for the Janus-1.3B and Pixtral-12B models, as reported in Fig. SM2. Both show the highest $\chi^{l,gt}$ for the internal image, with high initial values ($\chi^{l,gt} > 0.4$ and $\chi^{l,gt} > 0.2$ respectively) and lower signals coming from the [EOI] tokens.

The results presented above show that, in the Chameleon and Emu3, the [EOI] token is responsible for a large portion of cross-modal attention and contains the highest semantic information about the image. This makes it a suitable candidate for being a *narrow gate* of communication. In contrast, in the remaining models, the semantic content is more distributed throughout the whole image representation, suggesting that the model uses a much broader communication mechanism, relying on multiple regions of the image rather than a single token.

4.3. Ablation Experiments: The Effect of Localized Communication on Downstream Tasks

Building on the previous analysis, where we identified the token positions responsible for encoding visual features and those receiving the strongest attention during image-to-text communication, we now investigate their impact on performance across various vision-language benchmarks.

Specifically, we analyze how the ablation of these token

Model	Ablation	VQAv2	MS-COCO	Flickr	ImageNet
Chameleon-7B	-	0.51	0.48	0.34	0.46
	[EOI]	0.25	0.04	0.04	0.01
	img → text	0.40	0.27	0.17	0.47
Chameleon-34B	-	0.59	0.47	0.41	0.43
	[EOI]	0.39	0.01	0.01	0.00
	img → text	0.50	0.46	0.39	0.42
Emu3	-	0.57	0.63	0.29	0.35
	[EOI]	0.48	0.33	0.13	0.24
	img → text	0.42	0.54	0.21	0.30
Llava	-	0.80	0.98	0.70	0.5
	[EOI]	0.80	0.97	0.71	0.45
	img → text	0.00	0.01	0.02	0.05

Table 1. **Effect of Attention Knockout on Image Understanding Tasks.** Performance of Chameleon (7B and 34B) and Pixtral models on visual question answering (VQAv2), image captioning (Flickr-30k and MS-COCO), and image classification (ImageNet) under different attention ablation settings. The [EOI] ablation condition removes communication from the End of Image ([EOI]) token to text tokens. The “img → text” ablation blocks communication from all image tokens to text tokens while preserving communication from the [EOI] token to text. Numbers in bold mark the worst performance for each model and task.

position affects the responses of the VLMs to three standard benchmarks: VQAv2 [47] for visual question answering, Flickr30k [48] and MS-COCO [49] for image captioning. Details on the evaluation metrics for each task are provided in SM Sec. 7. In our ablations we block communication between [EOI] and text tokens, as well as between the residual streams of all visual and text tokens, by zeroing out respectively $A_{[EOI] \rightarrow \text{text}}$ and $A_{\text{img} \rightarrow \text{text}}$ (see Sec. 3.3 for additional details). To conduct this analysis, we first randomly sample 2000 data points from each dataset and establish performance baselines for each model. We then apply attention knockout to block communication from the residual streams of the [EOI] token and from all the image tokens to text.

The results for Chameleon, Emu3, and Llava are summarized in Tab. 1. For comparison, we also report the value of $\chi^{\text{out}, \text{gt}}$ on the ImageNet dataset at the output of the LLM on the last token of the prompt described in Sec. 4.2. The results for Pixtral, Janus and other special token positions, such as the last image token for the Chameleon models and the 1025th image token and [EOL] for Pixtral-12B, are provided in SM Sec. 6.3.

In Chameleon models, we observe a significant drop in performance across all four tasks when the communication between the residual stream at the [EOI] token position and the text is blocked. On VQAv2, the performance of Chameleon-7B decreases from 0.51 to 0.25, and in Chameleon-34B, it drops from 0.59 to 0.39. The decline is even more pronounced in captioning tasks and ImageNet. Chameleon-7B falls from a baseline of 0.34 on Flickr30k to 0.04 and Chameleon-34B drops from 0.41 to 0.01; on MS-

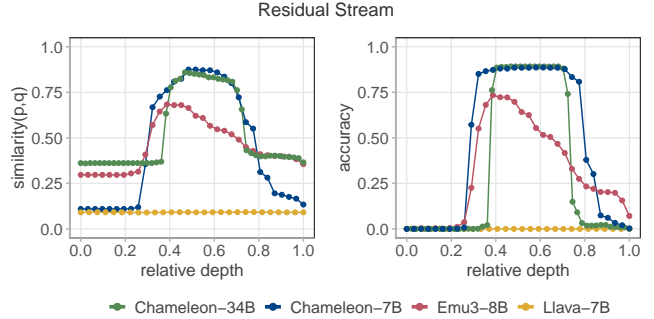


Figure 5. **Impact of Activation Patching at [EOI].** Results of patching the [EOI] representation on a target class onto the [EOI] representation on a base class. The experiment is performed at each layer. Two metrics are evaluated: (left) The Similarity (defined in Eq. (3)) measures how the probability distribution over the vocabulary of the patched image aligns with that of the target. (right) The accuracy, defined as the fraction of patched images where the probability of the target class token is larger than the probability of the base class token.

COCO, both Chameleon-7B and Chameleon-34B experience more than a 90% reduction from baseline performance. Similarly, ablating [EOI] on ImageNet reduces the overlap with the classes to almost zero. In the same way, in Emu3, the ablation of [EOI] decreases the performance by 50% on the captioning tasks from 0.57 to 0.48 in VQAv2 and from 0.35 to 0.24 on ImageNet. In contrast, when we ablate all the text-on-image attention weights by zeroing out $A_{\text{img} \rightarrow \text{text}}$, the drop in performance is smaller than the one caused by the ablation of [EOI] alone, with the only exception of VQAv2 on Emu3. Notably, in Chameleon-34B, ablating all the text-on-image attention block does not impact the model performance on captioning and ImageNet and it produces a decrease in VQAv2 accuracy from 0.59 to 0.50.

In Llava, the internal image-text communication channels are very different. While no significant performance drop is observed when blocking communication at the [EOI] token, the ablation of the text-on-image attention $A_{\text{img} \rightarrow \text{text}}$ completely disrupts performance, reaching 0.00 in VQAv2, 0.02 on Flickr30k, 0.01 on MS-COCO and 0.05 in ImageNet. Table SM2 in the SM shows that Pixtral and Janus behave similarly to Llava: their image-text communication is distributed across the internal image tokens and it does not rely on [EOI].

Overall, the results of our ablation experiments confirm that the cross-modal communication in Chameleon and Emu3 flows mainly through a *single* token, the special [EOI] token. On the contrary, in text-only output VLMs (Llava and Pixtral) and multimodal output models like Janus, that are fine-tuned for image understanding tasks, the communication happens in a distributed fashion through the image and it cannot be disrupted with a localized ablation.

4.4. Steering Image Understanding Through Activation Patching

So far, we have shown that in Chameleon and Emu3, $[\text{EOI}]$ encodes global information about the image (see Sec. 4.2), and it is the main communication gateway to text (see Sec. 4.3). In this section, we show that the localized nature of cross-modal communication in Chameleon-7B, Chameleon-34B, and Emu3 allows targeted editing of image semantics.

To do so, we perform a patching experiment selecting 20 animal classes from the ImageNet dataset, sampling 100 images from each class. We group the classes into ten pairs and construct the experiment as follows:

- i) we collect the $[\text{EOI}]$ representation at each layer l for the examples of one class of the pair, the target class $[\text{EOI}]^{l, \text{target}}$;
- ii) we intervene on the residual stream of images of the other class of the pair, which we call the base class. We replace $[\text{EOI}]^{l, \text{base}}$ by $[\text{EOI}]^{l, \text{target}}$ at selected layers;
- iii) we compute the probability distribution of the final token of the prompt and measure the alignment of the patched image with the target image.

The details on the prompt used and the selected classes are reported in SM Sec. 7. In this experiment, we set $[\text{EOI}]^{l^*, \text{base}}$ to $[\text{EOI}]^{l^*, \text{target}}$ in the residual stream. With this intervention, we modify the representation of $[\text{EOI}]$ of the base class for all the layers $l > l^*$ only indirectly, through the residual connections.

The left panel of Fig. 5 shows the effect of this patching on the similarity (according to the definition in Eq. (3)) between the probability distribution of the base class and that of the target class for Chameleon-7B (blue profile), Chameleon-34B (green), Emu3 (red) and Llava (yellow). In the initial layers, editing $[\text{EOI}]$ has no significant effect on $\text{Similarity}(q_{\text{base}}^{\text{patched}}, p_{\text{target}})$ since the information from the image has not reached $[\text{EOI}]$ yet. Indeed, in Sec. 4.2, Fig. 4 (left), we saw that $\chi^{l, \text{gt}}$ of $[\text{EOI}]$ grows between layers 5 and 10, both in Chameleon models and Emu3, which corresponds to a range of relative depths between 0.16 and 0.33. The patching of $[\text{EOI}]^{l^*, \text{target}}$ becomes more effective after a relative depth of 0.3 and the similarity reaches a peak of 0.86 in Chameleon-7B and Chameleon-34 and 0.70 for Emu3. After a relative depth of 0.7, the $\text{Similarity}(q_{\text{base}}^{\text{patched}}, p_{\text{target}})$ in Chameleon models decreases rapidly, returning to near-baseline levels at the last layer. This decrease suggests that most of the image information is passed to the last token position in the middle layers, in accordance with the findings of [27, 28]. The decrease is more gradual for the Emu model, suggesting that communication between $[\text{EOI}]$ and text occurs throughout the entire second half of the model. In the right panel of Fig. 5, we show, on average, how often the probability of the target class is higher than the base class after patching

$[\text{EOI}]^{l, \text{target}}$ into $[\text{EOI}]^{l, \text{base}}$. In Chameleon models, the intervention changes the class prediction from base to target 90% of times (see Fig. 5-right) while in Emu3 this happens 75% of the times.

We perform the same experiment on Llava, which presents distributed communication in absence of a “narrow gate”. The results clearly show that $[\text{EOI}]$ patching cannot steer the semantics of the image: the similarity between the distribution of the base and target class is unaffected by the patching of $[\text{EOI}]$, and the probability of the base class is always higher than that of the target ImageNet class (right panel). In Sec. 6.4 of the SM, we show that the behavior of Janus and Pixtral mirrors that of Llava, consistently with the results shown in Sec. 4.3 on the effect of $[\text{EOI}]$ ablation.

5. Conclusion

This study compares how information flows in early-fusion multimodal-output VLMs (e.g., Chameleon and Emu3) versus unimodal-output VLMs (e.g., Llava and Pixtral). In multimodal-output models, we observe that cross-modal communication is heavily localized, primarily passing through the $[\text{EOI}]$ token. By contrast – consistent with prior findings [27, 28] – unimodal-output models distribute this communication more evenly across multiple visual tokens. Interestingly, Janus exhibits a more diffuse communication pattern despite being a multimodal-output VLM. This suggests that text-aligned visual encoding combined with a text-pretrained backbone may be sufficient to suppress a tightly controlled “narrow gating” mechanism. Such localization in the $[\text{EOI}]$ token makes it easier to track how visual information influences text generation, providing greater transparency into a model’s decision-making. Moreover, when $[\text{EOI}]$ acts as a narrow gate, its ability to absorb visual information early means the original image tokens can be discarded afterward, reducing both memory usage and computational cost. However, the possibility of steering the model’s image semantics by modifying a single $[\text{EOI}]$ token presents both advantages and risks. On the one hand, it facilitates targeted image editing, content creation, and more efficient localized alignment (e.g., extending the approach in [65]). On the other hand, it introduces vulnerabilities to manipulation and bias. One potential safeguard against these issues is to encode the images with a CLIP-like encoder, which more robustly aligns text and image embeddings. Future research should explore whether these communication patterns appear in other multimodal-output VLMs and develop techniques to mitigate the potential risks associated with the controllability of the narrow gate.

Acknowledgments

The authors acknowledge the AREA Science Park supercomputing platform ORFEO made available for conducting

the research reported in this paper and the technical support of the Laboratory of Data Engineering staff. Alessandro Pietro Serra, Francesco Ortu, Emanuele Panizon, Lorenzo Basile, Alessio Ansuini, Diego Doimo and Alberto Cazzaniga were supported by the project “Supporto alla diagnosi di malattie rare tramite l’intelligenza artificiale” CUP: F53C22001770002 and “Valutazione automatica delle immagini diagnostiche tramite l’intelligenza artificiale”, CUP: F53C22001780002. Alessio Ansuini and Alberto Cazzaniga were supported by the European Union – NextGenerationEU within the project PNRR “PRP@CERIC” IR0000028 - Mission 4 Component 2 Investment 3.1 Action 3.1.1. Lucrezia Valeriani was supported by the project “QuB - Quantum Behavior in Biological Function” CUP: J95F21002820001.

References

- [1] Rishi Bommasani, Drew A. Hudson, Ehsan Adeli, Russ Altman, Simran Arora, Sydney von Arx, Michael S. Bernstein, Jeannette Bohg, Antoine Bosselut, Emma Brunskill, Erik Brynjolfsson, S. Buch, Dallas Card, Rodrigo Castellon, Niladri S. Chatterji, Annie S. Chen, Kathleen A. Creel, Jared Davis, Dora Demszky, Chris Donahue, Moussa Doumbouya, Esin Durmus, Stefano Ermon, John Etchemendy, Kawin Ethayarajh, Li Fei-Fei, Chelsea Finn, Trevor Gale, Lauren E. Gillespie, Karan Goel, Noah D. Goodman, Shelby Grossman, Neel Guha, Tatsunori Hashimoto, Peter Henderson, John Hewitt, Daniel E. Ho, Jenny Hong, Kyle Hsu, Jing Huang, Thomas F. Icard, Saahil Jain, Dan Jurafsky, Pratyusha Kalluri, Siddharth Karamcheti, Geoff Keeling, Fereshte Khani, O. Khattab, Pang Wei Koh, Mark S. Krass, Ranjay Krishna, Rohith Kudithipudi, Ananya Kumar, Faisal Ladhak, Mina Lee, Tony Lee, Jure Leskovec, Isabelle Levent, Xiang Lisa Li, Xuechen Li, Tengyu Ma, Ali Malik, Christopher D. Manning, Suvir P. Mirchandani, Eric Mitchell, Zanele Munyikwa, Suraj Nair, Avaniika Narayan, Deepak Narayanan, Benjamin Newman, Allen Nie, Juan Carlos Niebles, Hamed Nilforoshan, J. F. Nyarko, Giray Ogut, Laurel Orr, Isabel Papadimitriou, Joon Sung Park, Chris Piech, Eva Portelance, Christopher Potts, Aditi Raghunathan, Robert Reich, Hongyu Ren, Frieda Rong, Yusuf H. Roohani, Camilo Ruiz, Jack Ryan, Christopher R’e, Dorsa Sadigh, Shiori Sagawa, Keshav Santhanam, Andy Shih, Krishna Parasuram Srinivasan, Alex Tamkin, Rohan Taori, Armin W. Thomas, Florian Tramèr, Rose E. Wang, William Wang, Bohan Wu, Jiajun Wu, Yuhuai Wu, Sang Michael Xie, Michihiro Yasunaga, Jiaxuan You, Matei A. Zaharia, Michael Zhang, Tianyi Zhang, Xikun Zhang, Yuhui Zhang, Lucia Zheng, Kaitlyn Zhou, and Percy Liang. On the opportunities and risks of foundation models. *ArXiv*, 2021. [1](#)
- [2] Tom Brown, Benjamin Mann, Nick Ryder, Melanie Subbiah, Jared D Kaplan, Prafulla Dhariwal, Arvind Neelakantan, Pranav Shyam, Girish Sastry, Amanda Askell, Sandhini Agarwal, Ariel Herbert-Voss, Gretchen Krueger, Tom Henighan, Rewon Child, Aditya Ramesh, Daniel Ziegler, Jeffrey Wu, Clemens Winter, Chris Hesse, Mark Chen, Eric Sigler, Mateusz Litwin, Scott Gray, Benjamin Chess, Jack Clark, Christopher Berner, Sam McCandlish, Alec Radford, Ilya Sutskever, and Dario Amodei. Language models are few-shot learners. In H. Larochelle, M. Ranzato, R. Hadsell, M.F. Balcan, and H. Lin, editors, *Advances in Neural Information Processing Systems*, volume 33, pages 1877–1901. Curran Associates, Inc., 2020. [1](#)
- [3] Jonathan Berant, Andrew Chou, Roy Frostig, and Percy Liang. Semantic parsing on Freebase from question-answer pairs. In David Yarowsky, Timothy Baldwin, Anna Korhonen, Karen Livescu, and Steven Bethard, editors, *Proceedings of the 2013 Conference on Empirical Methods in Natural Language Processing*, pages 1533–1544, Seattle, Washington, USA, October 2013. Association for Computational Linguistics. [1](#)
- [4] Dzmitry Bahdanau, Kyunghyun Cho, and Yoshua Bengio. Neural machine translation by jointly learning to align and translate, 2016.
- [5] Mehdi Allahyari, Seyedamin Pouriyeh, Mehdi Assefi, Saeid Safaei, Elizabeth D. Trippe, Juan B. Gutierrez, and Krys Kochut. Text summarization techniques: A brief survey, 2017. [1](#)
- [6] Aditya Ramesh, Mikhail Pavlov, Gabriel Goh, Scott Gray, Chelsea Voss, Alec Radford, Mark Chen, and Ilya Sutskever. Zero-shot text-to-image generation, 2021. [1](#)
- [7] Chitwan Saharia, William Chan, Saurabh Saxena, Lala Li, Jay Whang, Emily L Denton, Kamyar Ghasemipour, Raphael Gontijo Lopes, Burcu Karagol Ayan, Tim Salimans, Jonathan Ho, David J Fleet, and Mohammad Norouzi. Photorealistic text-to-image diffusion models with deep language understanding. In S. Koyejo, S. Mohamed, A. Agarwal, D. Belgrave, K. Cho, and A. Oh, editors, *Advances in Neural Information Processing Systems*, volume 35, pages 36479–36494. Curran Associates, Inc., 2022.
- [8] Aditya Ramesh, Prafulla Dhariwal, Alex Nichol, Casey Chu, and Mark Chen. Hierarchical text-conditional image generation with clip latents, 2022. [1](#)
- [9] Amanpreet Singh, Ronghang Hu, Vedanuj Goswami, Guillaume Couairon, Wojciech Galuba, Marcus Rohrbach, and Douwe Kiela. Flava: A foundational language and vision alignment model. In *Proceedings of the IEEE/CVF Conference on Computer Vision and Pattern Recognition (CVPR)*, pages 15638–15650, June 2022. [1](#)
- [10] Jean-Baptiste Alayrac, Jeff Donahue, Pauline Luc, Antoine Miech, Iain Barr, Yana Hasson, Karel Lenc, Arthur Mensch, Katherine Millican, Malcolm Reynolds, Roman Ring, Eliza Rutherford, Serkan Cabi, Tengda Han, Zhitao Gong, Sina Samangooei, Marianne Monteiro, Jacob L Menick, Sebastian Borgeaud, Andy Brock, Aida Nematzadeh, Sahand Sharifzadeh, Mikołaj Bińkowski, Ricardo Barreira, Oriol Vinyals, Andrew Zisserman, and Karén Simonyan. Flamingo: a visual language model for few-shot learning. In S. Koyejo, S. Mohamed, A. Agarwal, D. Belgrave, K. Cho, and A. Oh, editors, *Advances in Neural Information Processing Systems*, volume 35, pages 23716–23736. Curran Associates, Inc., 2022. [2](#)
- [11] Haotian Liu, Chunyuan Li, Qingyang Wu, and Yong Jae Lee. Visual instruction tuning. In A. Oh, T. Naumann, A. Globerson, K. Saenko, M. Hardt, and S. Levine, editors, *Advances*

- in *Neural Information Processing Systems*, volume 36, pages 34892–34916. Curran Associates, Inc., 2023. 2
- [12] Matt Deitke, Christopher Clark, Sangho Lee, Rohun Tripathi, Yue Yang, Jae Sung Park, Mohammadreza Salehi, Niklas Muennighoff, Kyle Lo, Luca Soldaini, Jiasen Lu, Taira Anderson, Erin Bransom, Kiana Ehsani, Huong Ngo, Yen-Sung Chen, Ajay Patel, Mark Yatskar, Chris Callison-Burch, Andrew Head, Rose Hendrix, Favyen Bastani, Eli VanderBilt, Nathan Lambert, Yvonne Chou, Arnavi Chheda, Jenna Sparks, Sam Skjonsberg, Michael Schmitz, Aaron Sarnat, Byron Bischoff, Pete Walsh, Chris Newell, Piper Wolters, Tanmay Gupta, Kuo-Hao Zeng, Jon Borchardt, Dirk Groeneveld, Jen Dumas, Crystal Nam, Sophie Lebrecht, Caitlin Wittlif, Carissa Schoenick, Oscar Michel, Ranjay Krishna, Luca Weihs, Noah A. Smith, Hannaneh Hajishirzi, Ross Girshick, Ali Farhadi, and Aniruddha Kembhavi. Molmo and pixmo: Open weights and open data for state-of-the-art multimodal models, 2024.
- [13] Praveesh Agrawal, Szymon Antoniak, Emma Bou Hanna, Baptiste Bout, Devendra Chaplot, Jessica Chudnovsky, Diogo Costa, Baudouin De Monicault, Saurabh Garg, Theophile Gervet, Soham Ghosh, Amélie Héliou, Paul Jacob, Albert Q. Jiang, Kartik Khandelwal, Timothée Lacroix, Guillaume Lample, Diego Las Casas, Thibaut Lavril, Teven Le Scao, Andy Lo, William Marshall, Louis Martin, Arthur Mensch, Pavankumar Muddireddy, Valera Nemychnikova, Marie Pellat, Patrick Von Platen, Nikhil Raghuraman, Baptiste Rozière, Alexandre Sablayrolles, Lucile Saulnier, Romain Sauvestre, Wendy Shang, Roman Soletskyi, Lawrence Stewart, Pierre Stock, Joachim Studnia, Sandeep Subramanian, Sagar Vaze, Thomas Wang, and Sophia Yang. Pixtral 12b, 2024. 1, 2, 3
- [14] Christoph Schuhmann, Romain Beaumont, Richard Vencu, Cade Gordon, Ross Wightman, Mehdi Cherti, Theo Coombes, Aarush Katta, Clayton Mullis, Mitchell Wortsman, Patrick Schramowski, Srivatsa Kundurthy, Katherine Crowson, Ludwig Schmidt, Robert Kaczmarczyk, and Jenia Jitsev. Laion-5b: An open large-scale dataset for training next generation image-text models, 2022. 1
- [15] Hugo Laurençon, Lucile Saulnier, Léo Tronchon, Stas Bekman, Amanpreet Singh, Anton Lozhkov, Thomas Wang, Siddharth Karamcheti, Alexander M. Rush, Douwe Kiela, Matthieu Cord, and Victor Sanh. Obelics: An open web-scale filtered dataset of interleaved image-text documents, 2023. 1
- [16] Yuying Ge, Sijie Zhao, Ziyun Zeng, Yixiao Ge, Chen Li, Xintao Wang, and Ying Shan. Making LLaMA SEE and draw with SEED tokenizer. In *The Twelfth International Conference on Learning Representations*, 2024. 1, 2
- [17] Zineng Tang, Ziyi Yang, Chenguang Zhu, Michael Zeng, and Mohit Bansal. Any-to-any generation via composable diffusion. In A. Oh, T. Naumann, A. Globerson, K. Saenko, M. Hardt, and S. Levine, editors, *Advances in Neural Information Processing Systems*, volume 36, pages 16083–16099. Curran Associates, Inc., 2023. 1, 2
- [18] Gemini Team. Gemini: A family of highly capable multimodal models, 2024.
- [19] Jun Zhan, Junqi Dai, Jiasheng Ye, Yunhua Zhou, Dong Zhang, Zhigeng Liu, Xin Zhang, Ruibin Yuan, Ge Zhang, Linyang Li, Hang Yan, Jie Fu, Tao Gui, Tianxiang Sun, Yu-Gang Jiang, and Xipeng Qiu. AnyGPT: Unified multimodal LLM with discrete sequence modeling. In Lun-Wei Ku, Andre Martins, and Vivek Srikumar, editors, *Proceedings of the 62nd Annual Meeting of the Association for Computational Linguistics (Volume 1: Long Papers)*, pages 9637–9662, Bangkok, Thailand, August 2024. Association for Computational Linguistics. 1, 2
- [20] Chameleon Team. Chameleon: Mixed-modal early-fusion foundation models. *arXiv preprint arXiv:2405.09818*, 2024. 1, 2, 3
- [21] Runpei Dong, Chunrui Han, Yuang Peng, Zekun Qi, Zheng Ge, Jinrong Yang, Liang Zhao, Jianjian Sun, Hongyu Zhou, Haoran Wei, Xiangwen Kong, Xiangyu Zhang, Kaisheng Ma, and Li Yi. DreamLLM: Synergistic multimodal comprehension and creation. In *The Twelfth International Conference on Learning Representations*, 2024. 1, 2
- [22] Hong Chen, Xin Wang, Yuwei Zhou, Bin Huang, Yipeng Zhang, Wei Feng, Houlun Chen, Zeyang Zhang, Siao Tang, and Wenwu Zhu. Multi-modal generative ai: Multi-modal llm, diffusion and beyond, 2024. 1
- [23] Shenghao Xie, Wenqiang Zu, Mingyang Zhao, Duo Su, Shilong Liu, Ruohua Shi, Guoqi Li, Shanghang Zhang, and Lei Ma. Towards unifying understanding and generation in the era of vision foundation models: A survey from the autoregression perspective, 2024. 1
- [24] Quan Sun, Qiyang Yu, Yufeng Cui, Fan Zhang, Xiaosong Zhang, Yueze Wang, Hongcheng Gao, Jingjing Liu, Tiejun Huang, and Xinlong Wang. Emu: Generative pretraining in multimodality. In *The Twelfth International Conference on Learning Representations*, 2024. 1, 2
- [25] Shengqiong Wu, Hao Fei, Leigang Qu, Wei Ji, and Tat-Seng Chua. NExt-GPT: Any-to-any multimodal LLM. In *Forty-first International Conference on Machine Learning*, 2024. 1, 2
- [26] Xinlong Wang, Xiaosong Zhang, Zhengxiong Luo, Quan Sun, Yufeng Cui, Jinsheng Wang, Fan Zhang, Yueze Wang, Zhen Li, Qiyang Yu, Yingli Zhao, Yulong Ao, Xuebin Min, Tao Li, Boya Wu, Bo Zhao, Bowen Zhang, Liangdong Wang, Guang Liu, Zheqi He, Xi Yang, Jingjing Liu, Yonghua Lin, Tiejun Huang, and Zhongyuan Wang. Emu3: Next-token prediction is all you need, 2024. 1, 2, 3
- [27] Clement Neo, Luke Ong, Philip Torr, Mor Geva, David Krueger, and Fazl Barez. Towards interpreting visual information processing in vision-language models, 2024. 1, 3, 8
- [28] Samyadeep Basu, Martin Grayson, Cecily Morrison, Besmira Nushi, Soheil Feizi, and Daniela Massiceti. Understanding information storage and transfer in multi-modal large language models. In *The Thirty-eighth Annual Conference on Neural Information Processing Systems*, 2024. 3, 8
- [29] Yuxin Wen, Qingqing Cao, Qichen Fu, Sachin Mehta, and Mahyar Najibi. Efficient vision-language models by summarizing visual tokens into compact registers, 2024. 3
- [30] Matthew Trager, Pramuditha Perera, Luca Zancato, Alessandro Achille, Parminder Bhatia, and Stefano Soatto. Linear spaces of meanings: Compositional structures in vision-language models. In *ICCV*, pages 15349–15358, 2023. 1
- [31] Mikhail S. Burtsev, Yuri Kuratov, Anton Peganov, and Gregory V. Sapunov. Memory transformer, 2021. 2, 3

- [32] Junnan Li, Dongxu Li, Silvio Savarese, and Steven Hoi. BLIP-2: Bootstrapping language-image pre-training with frozen image encoders and large language models. In Andreas Krause, Emma Brunskill, Kyunghyun Cho, Barbara Engelhardt, Sivan Sabato, and Jonathan Scarlett, editors, *Proceedings of the 40th International Conference on Machine Learning*, volume 202 of *Proceedings of Machine Learning Research*, pages 19730–19742. PMLR, 23–29 Jul 2023. 2, 3
- [33] Peter Tong, Ellis Brown, Penghao Wu, Sanghyun Woo, Adithya Jairam Vedagiri IYER, Sai Charitha Akula, Shusheng Yang, Jihan Yang, Manoj Middepogu, Ziteng Wang, Xichen Pan, Rob Fergus, Yann LeCun, and Saining Xie. Cambrian-1: A fully open, vision-centric exploration of multimodal llms. In A. Globerson, L. Mackey, D. Belgrave, A. Fan, U. Paquet, J. Tomczak, and C. Zhang, editors, *Advances in Neural Information Processing Systems*, volume 37, pages 87310–87356. Curran Associates, Inc., 2024. 2
- [34] Yang Jin, Kun Xu, Kun Xu, Liwei Chen, Chao Liao, Jianchao Tan, Quzhe Huang, Bin CHEN, Chengru Song, dai meng, Di ZHANG, Wenwu Ou, Kun Gai, and Yadong MU. Unified language-vision pretraining in LLM with dynamic discrete visual tokenization. In *The Twelfth International Conference on Learning Representations*, 2024. 2
- [35] Quan Sun, Yufeng Cui, Xiaosong Zhang, Fan Zhang, Qiyang Yu, Yuezhe Wang, Yongming Rao, Jingjing Liu, Tiejun Huang, and Xinlong Wang. Generative multimodal models are in-context learners. In *Proceedings of the IEEE/CVF Conference on Computer Vision and Pattern Recognition (CVPR)*, pages 14398–14409, June 2024. 2
- [36] Chengyue Wu, Xiaokang Chen, Zhiyu Wu, Yiyang Ma, Xingchao Liu, Zizheng Pan, Wen Liu, Zhenda Xie, Xingkai Yu, Chong Ruan, et al. Janus: Decoupling visual encoding for unified multimodal understanding and generation. *arXiv preprint arXiv:2410.13848*, 2024. 2, 3
- [37] Yecheng Wu, Zhuoyang Zhang, Junyu Chen, Haotian Tang, Dacheng Li, Yunhao Fang, Ligeng Zhu, Enze Xie, Hongxu Yin, Li Yi, Song Han, and Yao Lu. VILA-u: a unified foundation model integrating visual understanding and generation. In *The Thirteenth International Conference on Learning Representations*, 2025. 2
- [38] Yuying Ge, Yixiao Ge, Ziyun Zeng, Xintao Wang, and Ying Shan. Planting a seed of vision in large language model, 2023. 2, 3
- [39] Aaron Van Den Oord, Oriol Vinyals, et al. Neural discrete representation learning. *Advances in neural information processing systems*, 30, 2017. 2
- [40] Oran Gafni, Adam Polyak, Oron Ashual, Shelly Sheynin, Devi Parikh, and Yaniv Taigman. Make-a-scene: Scene-based text-to-image generation with human priors. In Shai Avidan, Gabriel Brostow, Moustapha Cissé, Giovanni Maria Farinella, and Tal Hassner, editors, *Computer Vision – ECCV 2022*, pages 89–106, Cham, 2022. Springer Nature Switzerland. 2
- [41] Shengqiong Wu, Hao Fei, Xiangtai Li, Jiayi Ji, Hanwang Zhang, Tat-Seng Chua, and Shuicheng YAN. Towards semantic equivalence of tokenization in multimodal LLM. In *The Thirteenth International Conference on Learning Representations*, 2025. 3
- [42] Weixin Liang, Yuhui Zhang, Yongchan Kwon, Serena Yeung, and James Zou. Mind the gap: Understanding the modality gap in multi-modal contrastive representation learning. In Alice H. Oh, Alekh Agarwal, Danielle Belgrave, and Kyunghyun Cho, editors, *Advances in Neural Information Processing Systems*, 2022. 3
- [43] Timothée Darcet, Maxime Oquab, Julien Mairal, and Piotr Bojanowski. Vision transformers need registers. In *The Twelfth International Conference on Learning Representations*, 2024. 3
- [44] Liang Chen, Haozhe Zhao, Tianyu Liu, Shuai Bai, Junyang Lin, Chang Zhou, and Baobao Chang. An image is worth 1/2 tokens after layer 2: Plug-and-play inference acceleration for large vision-language models, 2024. 3
- [45] David M. Chan, Rodolfo Corona, Joonyong Park, Cheol Jun Cho, Yutong Bai, and Trevor Darrell. Analyzing the language of visual tokens, 2024. 3
- [46] Bo Li, Yuanhan Zhang, Dong Guo, Renrui Zhang, Feng Li, Hao Zhang, Kaichen Zhang, Yanwei Li, Ziwei Liu, and Chunyuan Li. Llava-onevision: Easy visual task transfer, 2024. 3
- [47] Yash Goyal, Tejas Khot, Douglas Summers-Stay, Dhruv Batra, and Devi Parikh. Making the V in VQA matter: Elevating the role of image understanding in Visual Question Answering. In *Conference on Computer Vision and Pattern Recognition (CVPR)*, 2017. 3, 7, 5
- [48] Peter Young, Alice Lai, Micah Hodosh, and Julia Hockenmaier. From image descriptions to visual denotations: New similarity metrics for semantic inference over event descriptions. *Transactions of the Association for Computational Linguistics*, 2:67–78, 2014. 3, 7, 5
- [49] Tsung-Yi Lin, Michael Maire, Serge Belongie, James Hays, Pietro Perona, Deva Ramanan, Piotr Dollár, and C. Lawrence Zitnick. Microsoft coco: Common objects in context. In David Fleet, Tomas Pajdla, Bernt Schiele, and Tinne Tuytelaars, editors, *Computer Vision – ECCV 2014*, pages 740–755, Cham, 2014. Springer International Publishing. 3, 7, 5
- [50] Olga Russakovsky, Jia Deng, Hao Su, Jonathan Krause, Sanjeev Satheesh, Sean Ma, Zhiheng Huang, Andrej Karpathy, Aditya Khosla, Michael Bernstein, et al. Imagenet large scale visual recognition challenge. *International journal of computer vision*, 115:211–252, 2015. 3, 5
- [51] Nelson Elhage, Neel Nanda, Catherine Olsson, Tom Henighan, Nicholas Joseph, Ben Mann, Amanda Askell, Yuntao Bai, Anna Chen, Tom Conerly, Nova DasSarma, Dawn Drain, Deep Ganguli, Zac Hatfield-Dodds, Danny Hernandez, Andy Jones, Jackson Kernion, Liane Lovitt, Kamal Ndousse, Dario Amodei, Tom Brown, Jack Clark, Jared Kaplan, Sam McCandlish, and Chris Olah. A mathematical framework for transformer circuits. *Transformer Circuits Thread*, 2021. <https://transformer-circuits.pub/2021/framework/index.html>. 3
- [52] Mor Geva, Jasmijn Bastings, Katja Filippova, and Amir Globerson. Dissecting recall of factual associations in autoregressive language models. In Houda Bouamor, Juan Pino, and Kalika Bali, editors, *Proceedings of the 2023 Conference on Empirical Methods in Natural Language Processing, EMNLP 2023, Singapore, December 6-10, 2023*, pages

- 12216–12235. Association for Computational Linguistics, 2023. 4
- [53] Diego Doimo, Aldo Glielmo, Alessio Ansuini, and Alessandro Laio. Hierarchical nucleation in deep neural networks. *Advances in Neural Information Processing Systems*, 33, 2020. 4
- [54] Atticus Geiger, Hanson Lu, Thomas Icard, and Christopher Potts. Causal abstractions of neural networks. In Marc’Aurelio Ranzato, Alina Beygelzimer, Yann N. Dauphin, Percy Liang, and Jennifer Wortman Vaughan, editors, *Advances in Neural Information Processing Systems 34: Annual Conference on Neural Information Processing Systems 2021, NeurIPS 2021, December 6-14, 2021, virtual*, pages 9574–9586, 2021. 4
- [55] Arthur Conmy, Augustine N. Mavor-Parker, Aengus Lynch, Stefan Heimersheim, and Adrià Garriga-Alonso. Towards automated circuit discovery for mechanistic interpretability. In Alice Oh, Tristan Naumann, Amir Globerson, Kate Saenko, Moritz Hardt, and Sergey Levine, editors, *Advances in Neural Information Processing Systems 36: Annual Conference on Neural Information Processing Systems 2023, NeurIPS 2023, New Orleans, LA, USA, December 10 - 16, 2023*, 2023. 4
- [56] Paul Jaccard. Distribution de la flore alpine dans le bassin des dranses et dans quelques régions voisines. *Bull Soc Vaudoise Sci Nat*, 37:241–272, 1901. 4
- [57] Facebook AI. Chameleon-7b. <https://huggingface.co/facebook/chameleon-7b>, 2024. 4
- [58] Facebook AI. Chameleon-30b. <https://huggingface.co/facebook/chameleon-30b>, 2024. 4
- [59] BAAI. Emu3-gen. <https://huggingface.co/BAAI/Emu3-Gen-hf>, 2025. 4
- [60] Llava-hf. Llava-onevision-7b. <https://huggingface.co/llava-hf/llava-onevision-qwen2-7b-ov-hf>, 2024. 4
- [61] Mistral Community. Pixtral-12b. <https://huggingface.co/mistral-community/pixtral-12b>, 2024. 4
- [62] DeepSeek AI. Janus-1.3b. <https://huggingface.co/deepseek-ai/Janus-1.3B>, 2024. 4
- [63] Maria d’Errico, Elena Facco, Alessandro Laio, and Alex Rodriguez. Automatic topography of high-dimensional data sets by non-parametric density peak clustering. *Information Sciences*, 560:476–492, 2021. 5, 6, 7
- [64] Andrew Rosenberg and Julia Hirschberg. V-measure: A conditional entropy-based external cluster evaluation measure. In Jason Eisner, editor, *Proceedings of the 2007 Joint Conference on Empirical Methods in Natural Language Processing and Computational Natural Language Learning (EMNLP-CoNLL)*, pages 410–420, Prague, Czech Republic, June 2007. Association for Computational Linguistics. 5
- [65] Emily Cheng, Marco Baroni, and Carmen Amo Alonso. Linearly controlled language generation with performative guarantees. *arXiv preprint arXiv:2405.15454*, 2024. 8
- [66] Emily Cheng, Diego Doimo, Corentin Kervadec, Iuri Maccocco, Jade Yu, Alessandro Laio, and Marco Baroni. Emergence of a high-dimensional abstraction phase in language transformers. *arXiv preprint arXiv:2405.15471*, 2024. 6
- [67] Diego Doimo, Alessandro Serra, Alessio Ansuini, and Alberto Cazzaniga. The representation landscape of few-shot learning and fine-tuning in large language models, 2024. 6
- [68] Stanislaw Antol, Aishwarya Agrawal, Jiasen Lu, Margaret Mitchell, Dhruv Batra, C. Lawrence Zitnick, and Devi Parikh. Vqa: Visual question answering. In *Proceedings of the IEEE International Conference on Computer Vision (ICCV)*, December 2015. 7
- [69] Ramakrishna Vedantam, C Lawrence Zitnick, and Devi Parikh. Cider: Consensus-based image description evaluation. In *Proceedings of the IEEE conference on computer vision and pattern recognition*, pages 4566–4575, 2015. 7

The Narrow Gate: Localized Image-Text Communication in Vision-Language Models

Supplementary Material

6. Additional Results

6.1. Modality Gap in VLMs

We extend the results of Sec. 4.1 to Janus and Pixtral. As illustrated in Fig. SM1, both models exhibit an alignment between modalities which grows along the model depth, similar to the behavior observed in LLaVA. Specifically, Fig. SM1-left confirms this alignment across modalities for both models. Additionally, Fig. SM1-right reveals that the homogeneity within modality clusters is lower compared to the Chameleon models and Emu3. This indicates that like LLaVA, Janus and Pixtral have a less pronounced modality gap.

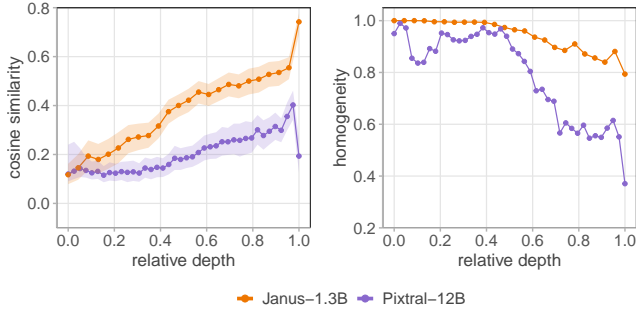


Figure SM1. **Modality Gap in VLMs.** (left) Cosine similarity between text and image token embeddings as a function of model depth reflects the orthogonality of modalities in Janus and Pixtral models. Points represent median cosine similarity, with shaded areas indicating the interquartile range. (right) Homogeneity score of token clusters generated via Advanced Density Peaks with respect to their original modality.

6.2. Cross-Modal Attention

The results for Chameleon-34B and Emu3 closely mirror those of Chameleon-7B, as discussed in Sec. 4.2. Fig. SM2-left visualizes the cross-modal attention contributions of image tokens, where tokens contributing more than 1% individually are shown explicitly, while the rest are grouped as "internal image". In Chameleon-34B, cross-modal attention is primarily concentrated on three tokens—[EOI], the first image token, and the last—whereas in Emu3, attention is dominated by [EOI] and tokens that encode the size of the image. In contrast, Janus and Pixtral exhibit a pattern similar to LLava (Sec. 4.2), where attention to special tokens remains low, while a significant portion of information is retained within internal image tokens. Fig. SM2-right further reveals that in both Chameleon-34B and Emu3, [EOI] consistently maintains high $\chi^{l,gt}$ values across layers, indicating its dominant role in encoding visual information. Meanwhile, all other tokens exhibit near-zero overlap values, suggesting minimal contribution to meaningful visual representation. For Janus, both [EOI] and internal image tokens carry strong information from the earliest layers, implying that visual encoding may be directly influencing their representations. However, as shown in Sec. 6.3, the information encoded in [EOI] does not appear to play a significant role in information flow within the backbone models.

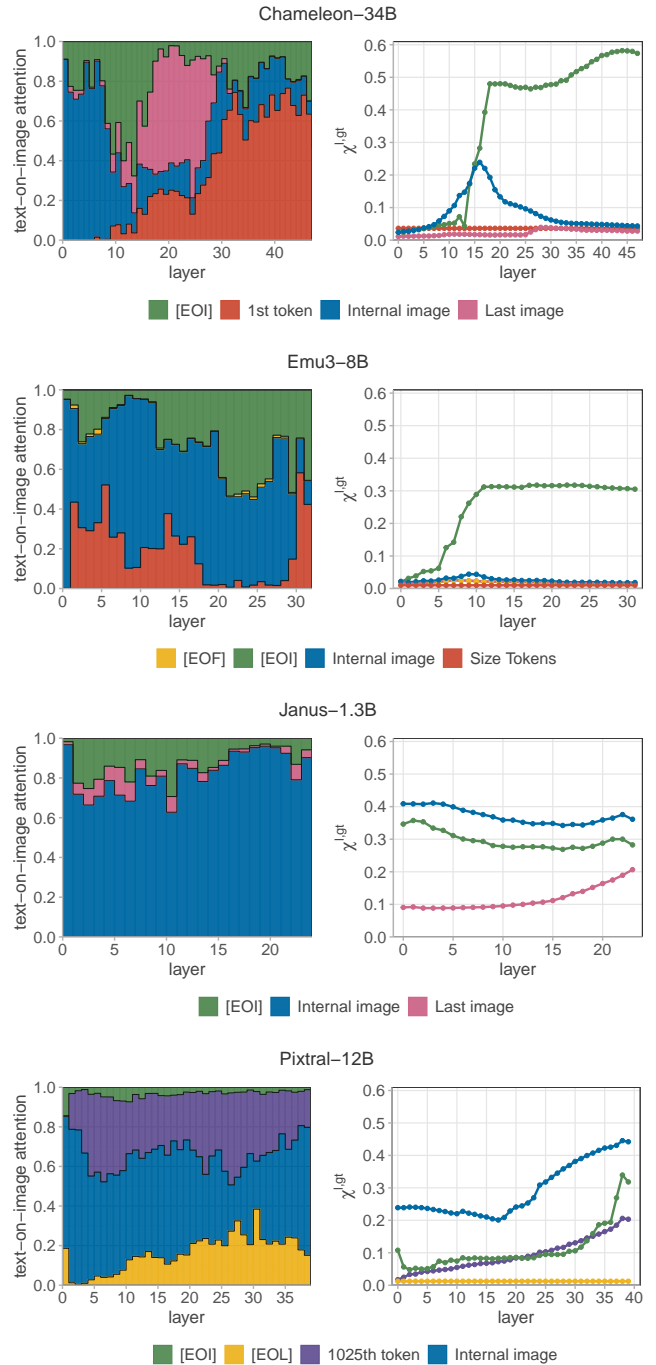


Figure SM2. **Localization of Information in Different Models.** Each row corresponds to a model. The left panel shows the contribution of image token positions to total text-on-image attention. The right panel presents the neighborhood overlap between selected image tokens and ImageNet labels.

6.3. Effect of attention knockout on vision-language tasks

Table SM2 extends the results of Table 1, showing the ablation effect on all tokens identified for their high cross-modal attention. The analysis further confirms that none of the special tokens, except for [EOI], play a significant role, as their ablation does not noticeably affects performance on any benchmarks.

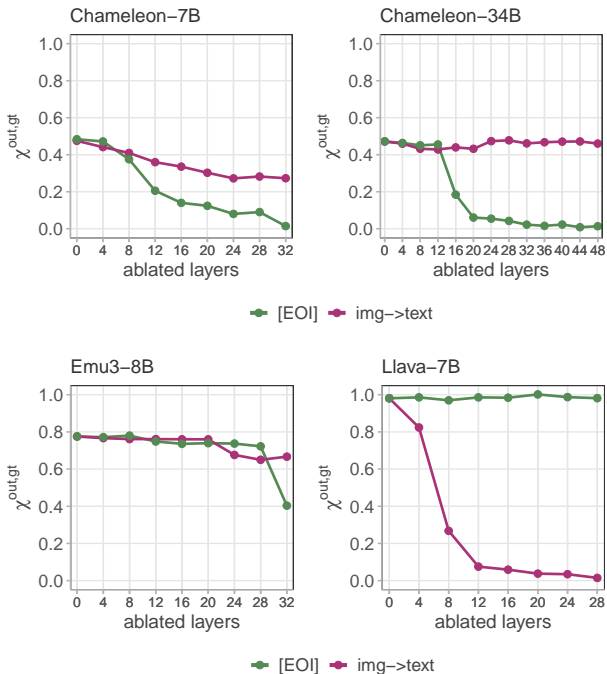


Figure SM3. **Effect of Progressive Attention Knockout.** CIDEr scores for the COCO captioning benchmark when ablating an increasing window of layers. The ablation intervention targets a range of layers, beginning from the final layer and proceeding backward, with two distinct conditions: blocking attention from the [EOI] token position to text tokens (green), and blocking attention from all image token positions to text tokens (magenta).

To obtain a more fine-grained understanding of ablation effects, we evaluated model performance on the COCO captioning benchmark while systematically ablating increasing windows of layers, starting from the final layers. Our experiments involved knocking out the attention either on the [EOI] token, and blocking communication between text and image modalities. For models in the Chameleon family, we observed that ablating the [EOI] token severely degraded performance even when only a few layers were affected, while removing image-to-text communication had minimal impact. In contrast, Emu3-8b showed more resilience to [EOI] token ablation, with significant performance deterioration occurring only when all layers were involved. Notably, for Emu3-8b, maintaining the [EOI] token was sufficient to

recover baseline performance even when image-to-text communication was blocked. Finally, as anticipated, Llava-7b exhibited behavior that was directly opposite to the Chameleon family models, confirming our hypothesis about architectural differences in cross-modal processing.

Model	Ablation	VQAv2	Flickr	MS-COCO	ImageNet ($\chi^{out,gt}$)
Chameleon-7B	-	0.51	0.34	0.48	0.46
	[EOI]	0.25	0.04	0.04	0.01
	Last-Image	0.42	0.20	0.32	0.46
	32nd	0.51	0.34	0.49	0.46
Chameleon-34B	-	0.59	0.41	0.47	0.43
	[EOI]	0.39	0.01	0.01	0.04
	Last-Image	0.58	0.39	0.46	0.41
	First-Image	0.57	0.38	0.46	0.42
Emu3	-	0.57	0.29	0.63	0.35
	[EOI]	0.48	0.13	0.32	0.24
	img → text	0.42	0.22	0.54	0.30
Llava-onevision	-	0.8	0.70	0.98	0.5
	[EOI]	0.8	0.71	0.97	0.45
	img → text	0.00	0.00	0.01	0.05
Pixtral	-	0.79	0.59	0.68	0.63
	[EOI]	0.77	0.62	0.68	0.61
	[EOLs]	0.76	0.54	0.61	0.61
	Last-Image	0.77	0.57	0.68	0.62
	1025	0.77	0.55	0.62	0.61
	img → text	0.37	0.00	0.01	0.06
Janus	-	0.51	0.32	0.43	0.65
	[EOI]	0.51	0.32	0.42	0.65
	img → text	0.00	0.01	0.01	0.06

Table SM2. **Effect of Attention Knockout on Image Understanding Tasks.** Performance of the models on visual question answering (VQAv2), image captioning (Flickr-30k and MS-COCO), and image classification (ImageNet) under different attention ablation settings. Depending on the model, we ablated the special tokens with high cross-modality attention by removing their communication with the text tokens. Numbers in bold mark the worst performance for each model and task.

6.4. Steering Image Understanding Through Activation Patching

We extended the experiments described in Section 4.4 to the Janus-1.3b and Pixtral-12b models, reproducing Figure 5 for these additional architectures. Our results reveal that in these models patching the residual stream of [EOI] does not influence the logit distribution.

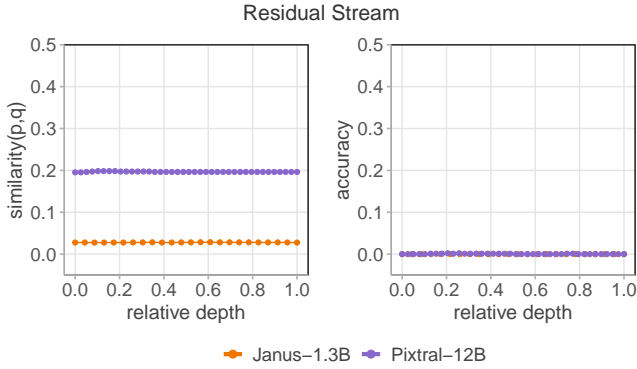


Figure SM4. **Impact of Activation Patching at [EOI] in Pixtral-12b and Janus-1.3b** Results of patching the [EOI] representation from a target class onto the [EOI] representation on a base class. The experiment is performed at each layer. **(left)** The Similarity (defined in Eq. (3)) measures how the probability distribution over the vocabulary of the patched image aligns to that of the target. **(right)** The accuracy, defined as the fraction of patched images where the probability of the target class token is larger than the probability of the base class token.

7. Experimental Setup

7.1. Finetuning details

We fine-tuned Emu3 on a mixture of datasets using 37.5k samples from the VQAy2 [47] and MS-COCO-2014 [49] training sets and 150k samples the Llava-instruct-150K using the [Hugging Face](#) implementation. We finetuned Emu3 with LoRA for one epoch using a batch size of 64, Adam optimizer without weight decay, and cosine annealing scheduler starting with a learning rate of 5e-5.

7.2. Model Used

Tab. SM3 shows the detailed configurations of each model employed in the experiments.

7.3. Image-text prompt constructed from Flickr-30k

The Flickr-30k [48] dataset comprises 30,000 images, each associated with five captions. To generate prompts that alternate between text-first and image-first formats, we structured the inputs by concatenating all five captions for each image, either preceding or following the image itself, depending on the intended sequence.

7.4. Image-text prompt constructed from ImageNet

For all experiments involving ImageNet images, we use a consistent subset of the dataset. We randomly select 100 animal classes and sample 100 images from each class, yielding 10,000 images. The selected classes are:

- staffordshire_bullterrier.n.01
- otterhound.n.01
- appenzeller.n.01
- chow.n.03
- hornbill.n.01
- basenji.n.01
- australian_terrier.n.01
- chesapeake_bay_retriever.n.01
- irish_setter.n.01
- scotch_terrier.n.01
- red_wolf.n.01
- american_staffordshire_terrier.n.01
- labrador_retriever.n.01
- standard_poodle.n.01
- lakeland_terrier.n.01
- saluki.n.01
- thunder_snake.n.01
- platypus.n.01
- dragonfly.n.01
- rhodesian_ridgeback.n.01
- spiny_lobster.n.02
- chambered_nautilus.n.01
- komondor.n.01
- collie.n.01

- egyptian_cat.n.01
- leonberg.n.01
- vizsla.n.01
- flat_coated_retriever.n.01
- fiddler_crab.n.01
- eskimo_dog.n.01
- affenpinscher.n.01
- boston_bull.n.01
- samoyed.n.03
- dungeness_crab.n.02
- french_bulldog.n.01
- groenendael.n.01
- bee_eater.n.01
- snow_leopard.n.01
- toy_terrier.n.01
- killer_whale.n.01
- entlebucher.n.01
- spotted_salamander.n.01
- mexican_hairless.n.01
- chihuahua.n.03
- ruffed_grouse.n.01
- giant_schnauzer.n.01
- brittany_spaniel.n.01
- brabancon_griffon.n.01
- pekinese.n.01
- cocker_spaniel.n.01
- loggerhead.n.02
- pembroke.n.01
- agama.n.01
- black_and_gold_garden_spider.n.01
- ostrich.n.02
- sealyham_terrier.n.01
- bernese_mountain_dog.n.01
- maltese_dog.n.01
- black_and_tan_coonhound.n.01
- redbone.n.01
- spider_monkey.n.01
- welsh_springer_spaniel.n.01
- admiral.n.02
- komodo_dragon.n.01
- borzoi.n.01
- briard.n.01
- bluetick.n.01
- norwegian_elkhound.n.01
- macaw.n.01
- great_dane.n.01
- greater_swiss_mountain_dog.n.01
- hermit_crab.n.01
- tailed_frog.n.01
- tench.n.01
- bloodhound.n.01
- german_short_haired_pointer.n.01
- tree_frog.n.02

Parameters	Chameleon-7B	Chameleon-34B	Emu3	Llava-onevision	Pixtral	Janus
N. Parameters	7B	34B	8B	7B	12B	1.3B
Visual Encoder	VQ-GAN	VQ-GAN	VQ-GAN	SigLIP	Pixtral-ViT	Sig-LIP/VQ-GAN
Image Generation	Yes	Yes	Yes	No	No	Yes
N. Layers	32	48	32	28	40	24
N. Attention Heads	32	48	32	28	32	16
Hidden Dim.	4096	8192	4096	3584	5120	2048

Table SM3. **Comparison of Model Architectures.** Detailed configurations of each model, including parameters, visual encoders, generation capabilities, layer counts, attention heads, and hidden dimensions.

- soft-coated_wheaten_terrier.n.01
- green_lizard.n.01
- alligator_lizard.n.01
- ringneck_snake.n.01
- persian_cat.n.01
- sidewinder.n.01
- italian_greyhound.n.01
- bedlington_terrier.n.01
- puffer.n.02
- bull_mastiff.n.01
- miniature_pinscher.n.01
- shetland_sheepdog.n.01
- red-breasted_merganser.n.01
- beagle.n.01
- banded_gecko.n.01
- white_wolf.n.01
- african_elephant.n.01
- arabian_camel.n.01
- indigo_bunting.n.01
- miniature_schnauzer.n.01
- irish_terrier.n.01
- peacock.n.02
- kelpie.n.02

For the activation patching experiment, described in Sec. 4.4, we manually select 20 class from the list above to ensure semantic diversity in the animal represented, and then we random sample 100 images for each class, obtaining a total of 2000 images. The selected pairs are:

- (american_alligator.n.01, arabian_camel.n.01)
- (bald_eagle.n.01, barn_spider.n.01)
- (bee_eater.n.01, cheetah.n.01)
- (flamingo.n.01, great_grey_owl.n.01)
- (green_mamba.n.01, grey_whale.n.01)
- (hippopotamus.n.01, jaguar.n.01)
- (king_penguin.n.01, kit_fox.n.01)
- (lionfish.n.01, macaw.n.01)
- (proboscis_monkey.n.01, siberian_husky.n.01)
- (tailed_frog.n.01, trilobite.n.01)

Then for the experiment described in Sec. 4.2, Sec. 4.3 we use the following prompt construction “<image>

This animal is a”. For the activation patching experiment described in Sec. 4.4 we use the same prompt for Chameleon-7B. For Chameleon-34B, we adopt a slightly modified prompt: “<image> Answer the question using a single word, number, or short phrase. This animal is a” as Chameleon-34B refused to respond to the original prompt.

7.5. Advanced density peaks clustering.

The Advanced Density Peaks (ADP) clustering [63] is a mode-seeking, density-based clustering algorithm that finds the modes of the probability density on the data’s low-dimensional data without performing any explicit dimensional reduction. We summarize the main steps below and refer the interested reader to the original paper [63].

The algorithm consists of three steps: the estimation of the data’s intrinsic dimension, the estimation of the local density around each point, and a final density-based clustering of the data. Following previous works [66, 67], we estimate the intrinsic dimension with `GrIde`, a neighbor-based intrinsic dimension estimator, setting the rank k of the nearest neighbor involved in the estimate to 16 (see [67] for more details). We then measure the local density around each data point with a k NN approach: $\rho_{i,k} = \frac{k}{NV_k}$. Here, N is the number of data points, and V is the volume of the ball, which has a radius equal to the distance between the point i and its k^{th} nearest neighbor. Importantly, we measure the volume on the intrinsic manifold using the intrinsic dimension value estimated in the first step.

The third step is the density-based clustering. With the knowledge of the ρ_i , we find a collection of density peaks $\mathcal{C} = \{c^1, \dots, c^n\}$, assign the data points around them, and find the density $\rho^{\alpha,\beta}$ of saddle points between a pair of clusters c_α c_β with the procedure described in [63]. The statistical reliability of the peaks is assessed with a t -test on $\log \rho^\alpha - \log \rho^{\alpha,\beta}$, where ρ^α is the maximum density of peak c_α , and $\rho^{\alpha,\beta}$ the density of the saddle point between c_α and c_β . Once the confidence level Z is fixed, all the clusters that do not pass the t -test are merged since the value of their density peaks are considered indistinguishable from the nearby saddle point. The process is repeated until all the peaks satisfy the t -test and are statistically robust with a

confidence Z [63].

In the analysis reported in Sec. 4.1 we remove clusters with size lower than 50.

7.6. Metrics

VQA accuracy. The Visual Question Answering (VQA) [68] benchmark relies on annotations provided by 10 Amazon Mechanical Turk workers for each image-question pair, with the most frequently given answer designated as the ground truth. The evaluation metric, denoted as $\text{Acc}(\text{ans})$, is defined as follows:

$$\text{Acc}(\text{ans}) = \min \left\{ \frac{\#\text{humans that said ans}}{3}, 1 \right\}.$$

This formulation ensures robustness by weighting answers based on consensus among annotators, capping the contribution of an answer to the accuracy score at 1.0. Before evaluating the answers provided by the models, both ground truth and predicted answers are preprocessed to standardize formatting and mitigate discrepancies arising from superficial variations; for further information, we refer to the VQA evaluation script². These steps include:

1. **Lowercasing:** All characters are converted to lowercase.
2. **Period Handling:** Periods are removed unless they appear in decimal numbers.
3. **Numerical Normalization:** Number words are converted to digits.
4. **Article Removal:** Articles (“a,” ”an,” ”the”) are omitted.
5. **Contraction Normalization:** Missing apostrophes in contractions are restored (e.g., “dont” becomes “don’t”).
6. **Punctuation Handling:**
 - Most punctuation marks are replaced with a space, except apostrophes and colons.
 - Apostrophes are preserved to avoid altering possessive forms.
 - Colons are retained for time-related references.
 - Commas between digits are removed without inserting spaces (e.g., “100,978” becomes “100978”).

CIDEr For the captioning benchmarks on Flickr [48] and MS COCO [49], we used CIDEr [69] metric. This metric assesses the quality of image captions by comparing a candidate sentence c_i to a set of reference sentences $\mathcal{R}_i = \{\mathbf{r}_{i1}, \dots, \mathbf{r}_{im}\}$ associated with an image I_i . The CIDEr metric evaluates candidate sentences by representing both the candidate and reference sentences as n -grams, which are sequences of 1-4 words reduced to their root forms (e.g., “fishing,” “fished,” and “fishes” become “fish”). To measure their relevance, a Term Frequency-Inverse Document Frequency (TF-IDF) weighting is employed where

Term Frequency (TF) captures the frequency of an n -gram ω_k within a sentence, and Inverse Document Frequency (IDF) discounts n -grams that are common across the dataset, for the explicit formula we refer to the original paper [69]

Using these weights, the metric calculates the cosine similarity between the TF-IDF-weighted n -gram vectors of the candidate sentence and the reference sentences, capturing their alignment. This similarity is expressed as:

$$\text{CIDEr}_n(c_i, \mathcal{R}_i) = \frac{1}{m} \sum_j \frac{\mathbf{g}^n(c_i) \cdot \mathbf{g}^n(\mathbf{r}_{ij})}{\|\mathbf{g}^n(c_i)\| \|\mathbf{g}^n(\mathbf{r}_{ij})\|},$$

where \mathbf{g}^n represents the TF-IDF-weighted vector for n -grams. The CIDEr score aggregates these similarity scores across n -grams of different lengths, combining them with equal weights for $n \in \{1, 2, 3, 4\}$ as follows:

$$\text{CIDEr}(c_i, \mathcal{R}_i) = \frac{1}{4} \sum_{n=1}^4 \text{CIDEr}_n(c_i, \mathcal{R}_i).$$

²<https://github.com/GT-Vision-Lab/VQA/tree/master>